JMEPEG (2009) 18:863–870
DOI: 10.1007/s11665-008-9322-5

1059-9495/$19.00

Simulation of High-Temperature AA5083 Bulge Forming with a Hardening/Softening Material Model

F.S. Jarrar, F.K. Abu-Farha, L.G. Hector Jr., and M.K. Khraisheh

(Submitted July 17, 2008)

High-temperature bulge forming of AA5083 aluminum sheet was simulated with the commercial finite element (FE) code ABAQUS™. A material model that is strain rate sensitive and accounts for strain hardening and softening was used. Results were compared with data from AA5083 bulge forming experiments at 450 °C where the gas pressure was a prescribed constant value. The results show that the material model is capable of predicting the deformation and thinning behavior at different constant pressure levels. In ancillary simulations, time-varying pressure profiles were computed (rather than prescribed) with an internal ABAQUS™ routine that attempts to maintain the strain rate at the bulge dome pole within a specified range. The time-varying profiles, for which no experimental AA5083 bulge forming data exist, can be programmed into existing bulge testing instrumentation to validate the associated predictions of bulge dome height and thinning. The present effort represents a necessary step toward predicting gas pressure profiles by coupling the pressure profile with a desired sheet deformation rate.

Keywords AA5083, bulge forming, quickplastic forming, superplastic forming

1. Introduction

High-temperature gas pressure bulge forming of nonferrous sheet materials is a useful means for evaluating material formability under a biaxial stress state. A substantial body of theoretical and experimental literature aimed at understanding material deformation in bulge forming has appeared over the past several decades due in large part to its relative simplicity (e.g. zero or minimal friction, axisymmetric geometry, thin sheet material, gas pressure loading) (Ref 1-11). Bulge forming is often used to evaluate Al alloy formability, such as AA5083, for use in quickplastic forming (QPF) of complex body closure panels (Ref 12). The faster forming rates and lower forming temperatures associated with QPF provide substantial advantages over conventional superplastic forming (SPF) processes (Ref 12).

In this article, we used the finite element (FE) code ABAQUS™ (Ref 13, 14) to investigate AA5083 hardening/softening in bulge forming under QPF conditions with a single-term material model. This model accounts for strain rate sensitivity, strain hardening and softening, and the evolution of state variables that can represent grain growth and cavitation. Results from the FE model were compared with existing AA5083 experimental bulge forming data wherein the gas pressure was prescribed to follow a constant value during forming. A series of ancillary FE calculations was conducted in which time-varying gas pressure profiles, based on a constant effective strain rate at the dome pole, were predicted (rather than prescribed) using a pressure control algorithm internal to ABAQUS™ (Ref 14). This represents a necessary step toward prediction of gas pressure profiles that can reduce QPF cycle times below what they are with current profiles without adversely affecting thinning.

F.S. Jarrar, F.K. Abu-Farha, and **M.K. Khraisheh**, Center for Manufacturing and Mechanical Engineering Department, University of Kentucky, Lexington, KY; **L.G. Hector Jr.**, General Motors R&D Center, Warren, MI; and **M.K. Khraisheh**, Masdar Institute of Science and Technology, Abu Dhabi, United Arab Emirates. Contact e-mails: fsjarr0@engr.uky.edu and khraisheh@engr.uky.edu.

2. AA5083 Material Models

2.1 AA5083 450 °C Uniaxial Tensile Data

High-temperature (450 °C) AA5083 tensile data reported in Ref 15 were used to fit a single-term material model introduced in the next section. The tensile data, which were measured at strain rates ranging from 0.0005 to 0.3 s^{-1}, are shown in Fig. 1 as true stress (MPa) versus true strain. A yield point effect (or local increase in the flow stress at small strains) appears at 0.01 s^{-1}. At the largest effective strain rates of 0.1 and 0.3 s^{-1}, the material appears to soften beyond the yield point, although necking probably occurred not long after the yield point in the tensile tests.

2.2 Constitutive Equations

To capture the AA5083 strain softening/hardening behavior over the range of strain rates shown in Fig. 1, a single-term phenomenological constitutive model was used in the FE simulations:

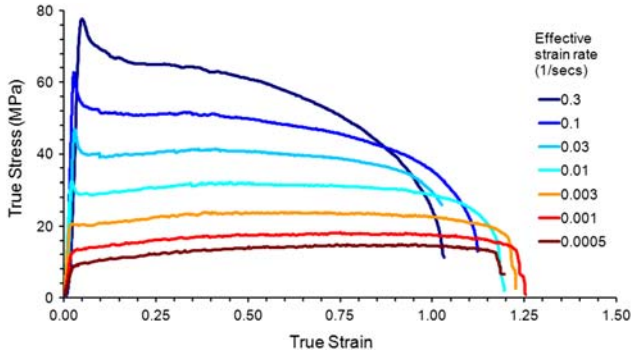

Fig. 1 True stress versus true strain curves for AA5083 at 450 °C from tensile tests (Ref 15)

Table 1 Parameters resulting from the fit to Eq 1-3

Parameter	Value
n	0.5
P	$-3 - 0.43 \ln(\dot{\bar{\varepsilon}})$
$\ln(K)$	$-15.251 - 0.2021 \ln(\dot{\bar{\varepsilon}}) + 0.0346 \ln^2(\dot{\bar{\varepsilon}})$
d_0, μm	8.0
C	2.5
f_{a_0}, %	1.25
ψ	1.5

$$\dot{\bar{\varepsilon}} = \frac{K}{d^P}\left(\frac{\bar{\sigma}}{1 - f_a}\right)^{1/n} \quad \text{(Eq 1)}$$

$$d = d_0 + c\bar{\varepsilon} \quad \text{(Eq 2)}$$

$$f_a = f_{a_0} \exp(\psi\bar{\varepsilon}) \quad \text{(Eq 3)}$$

This model has been previously applied in FE simulations of SPF processes of both Al and Mg alloy sheets (Ref 16-18). Note that $\bar{\varepsilon}$ and $\dot{\bar{\varepsilon}}$ are the von Mises effective strain and strain rate, respectively, $\bar{\sigma}$ is the von Mises effective flow stress, n is a constant which is not equal to the strain rate sensitivity, d is the average grain size, d_0 is the initial grain size (~8.0 μm), f_{a_0} and f_a are the initial and current area fraction of voids, respectively, ψ is the void growth parameter, and p and K are state variables that are functions of the effective strain rate. To account for the change in microstructure during deformation, evolution equations for grain size (d) and area fraction of voids (f_a) are used. A simple linear grain growth model similar to the one used by Caceres and Wilkinson (Ref 19) is used here. Use of the cavitation evolution model described by the exponential relation in Eq 3 is based upon the assumption that cavitation is primarily controlled by the plastic flow of the surrounding matrix (Ref 20-22).

Using a fitting process detailed elsewhere (Ref 16-18), the parameters listed in Table 1 were computed for Eq 1-3. Note that the values of d_0, c, f_{a_0}, n and ψ were chosen based on the literature since no experimental data on the microstructural evolution in the material were available (Ref 23-26).

Figure 2 shows a plot of the material model against the experimental data in Fig. 1. The seemingly straight lines (each is actually a curve) represent the fit results in stress-strain space to the experimental data.

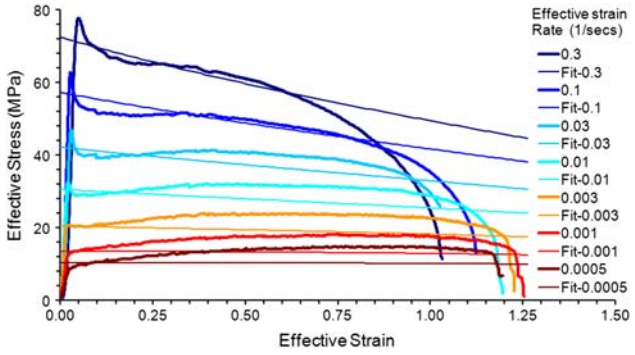

Fig. 2 Comparison of the material model Eq 1-3, with fit parameters/functions in Table 1 (straight lines denoted with "–Fit" in the key) and the AA5083 450 °C tensile data (Ref 15)

3. Finite element analysis (FEA)

The FE model is based upon the bulge forming instrumentation detailed in Ref 3: this is shown in Fig. 3. The sheet is clamped along the die flange, as shown in Fig. 3(a) and (b), and the sheet/die combination is heated to 450 °C prior to gas pressure application. The die has a 100-mm inner diameter, a 150-mm diameter flange, and a 5-mm fillet radius. One-half of the die is shown in section view in Fig. 3(c). The circular sheet has a 114 mm diameter and initial thickness of 1.2 mm. The sheet was meshed using 3D membrane elements, whereas the die was meshed using 3D rigid elements. The sheet nodes located along the sheet circumference were fixed. All simulations were conducted with the implicit solver in the commercial FE code ABAQUS™ 6.6.1 (Ref 13). The creep response was defined in a user-material subroutine containing the material model. Zero friction was assumed at the die entry radius.

Two sets of FE simulation runs were performed. In the first set, a constant gas pressure was prescribed during bulge forming. In the second set of FE simulations, the gas pressure profile was computed (rather than prescribed at the outset of the simulation) using an algorithm internal to ABAQUS™ 6.6.1 (Ref 14). During each increment, the ratio (r) of the maximum equivalent creep strain rate ($\dot{\bar{\varepsilon}}_{max}$), in a chosen element set, to the target creep strain rate ($\dot{\bar{\varepsilon}}_{tar}$), specified by the user, is calculated:

$$r = \frac{\dot{\bar{\varepsilon}}_{max}}{\dot{\bar{\varepsilon}}_{tar}} \quad \text{(Eq 4)}$$

If $0.2 \le r \le 3.0$, the increment is accepted and the pressure is adjusted as follows:

If $0.2 \le r < 0.5$ then $P_{new} = 1.5P_{old}$
If $0.5 \le r < 0.8$ then $P_{new} = 1.2P_{old}$
If $0.8 \le r < 1.5$ (target range) then $P_{new} = P_{old}$
If $1.5 \le r \le 3.0$ then $P_{new} = 0.834P_{old}$ where P_{new} is the new pressure magnitude and P_{old} is the old pressure magnitude.

However, if $r < 0.2$ or $r > 3.0$ in any given increment, the increment is abandoned and restarted according to the following logic:

If $r < 0.2$ then $P_{new} = 2P_{old}$
If $r > 3.0$ then $P_{new} = 0.5P_{old}$

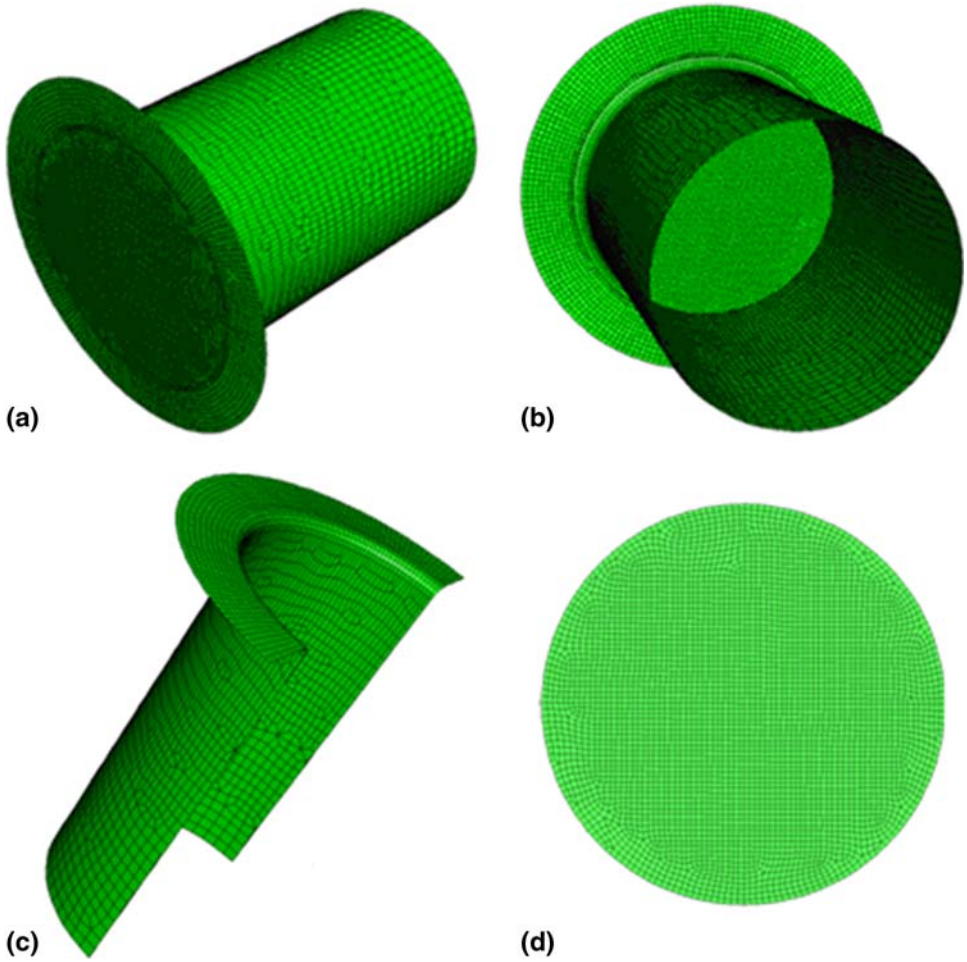

Fig. 3 (a, b) Different views of the die and sheet meshes together, (c) one-half of the die mesh shown in section view, and (d) sheet mesh alone

The ABAQUS™ pressure control algorithm was not expected to precisely meet the target effective strain rate value due to the ranges set for *r*. However, it is one of the most rudimentary approaches to gas pressure prediction in which the instantaneous gas pressure is coupled to the deformation rate at a specific location in the sheet (the dome pole in this case). We note that other approaches to predicting gas pressure profiles in SPF processes based on a target effective strain rate are detailed in Ref 27, 28. Also, the pressure control algorithms in ABAQUS™ and LS-DYNA have been compared in Ref 29 for SPF. The variation of the ratio *r* predicted with the ABAQUS™ routine was reported to be less than that using LS-DYNA.

4. Results and Discussion

4.1 Constant Pressure Bulge Forming

Three constant gas pressures were investigated, viz., 0.290 MPa (42 psi), 0.56 MPa (81 psi), 0.90 MPa (130 psi). Figure 4 shows a fully formed hemispherical AA5083 dome at 1078 s forming time due to a constant gas pressure of 0.29 MPa (42 psi). Color contours of constant displacement (mm) relative to the die flange are shown in the FE mesh on the dome with displacement values listed in the key. The peak dome pole displacement is 50.0 mm.

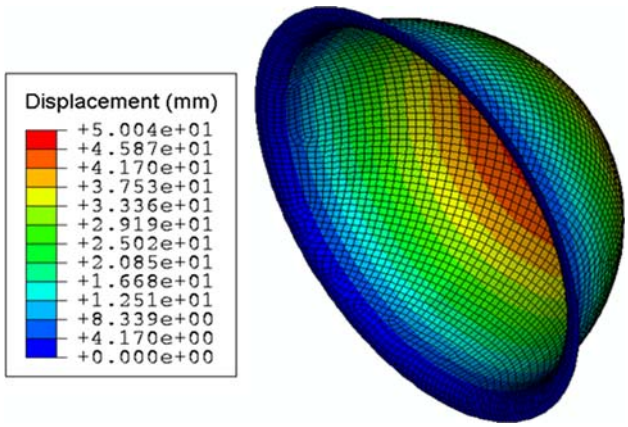

Fig. 4 Representative AA5083 bulge dome shape computed at 450 °C and a 0.290 MPa (42 psi) constant pressure. Displacement values listed in the key correspond to color contours in the FE mesh and are normal to the die flange in Fig. 3. Initial sheet thickness is 1.2 mm. Forming was terminated when the dome displacement reached 50.0 mm

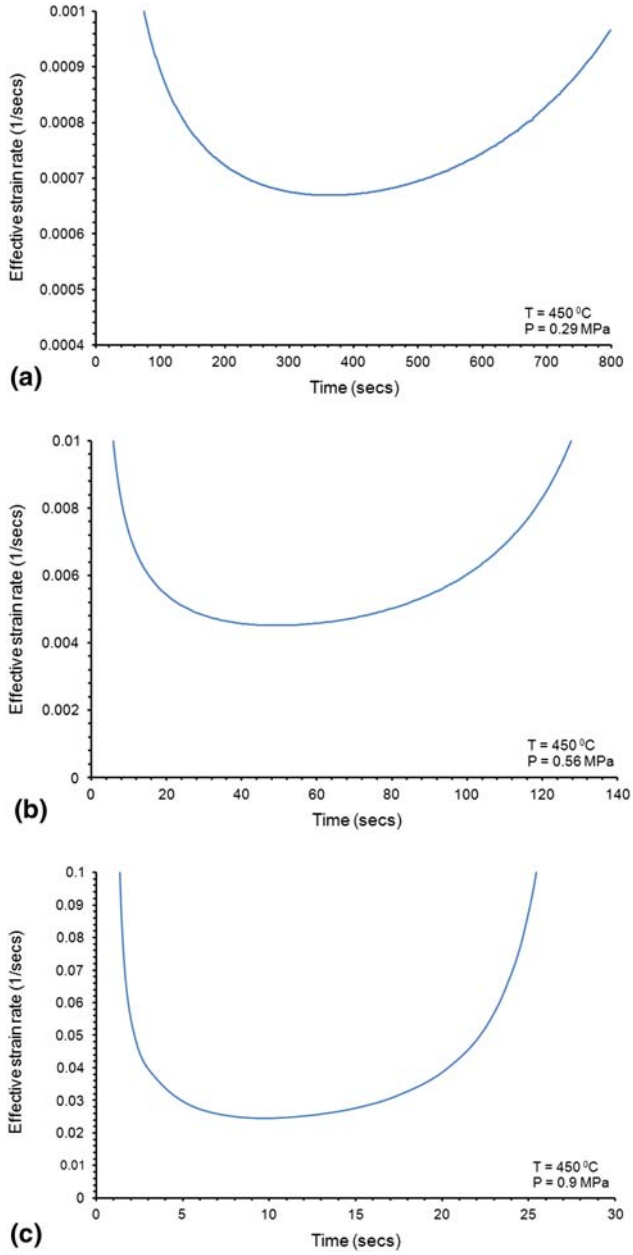

Fig. 5 Evolution of effective strain rate at the dome pole for AA5083 at 450 °C: (a) 0.29 MPa (42 psi), (b) 0.56 MPa (81 psi), and (c) 0.90 MPa (130 psi)

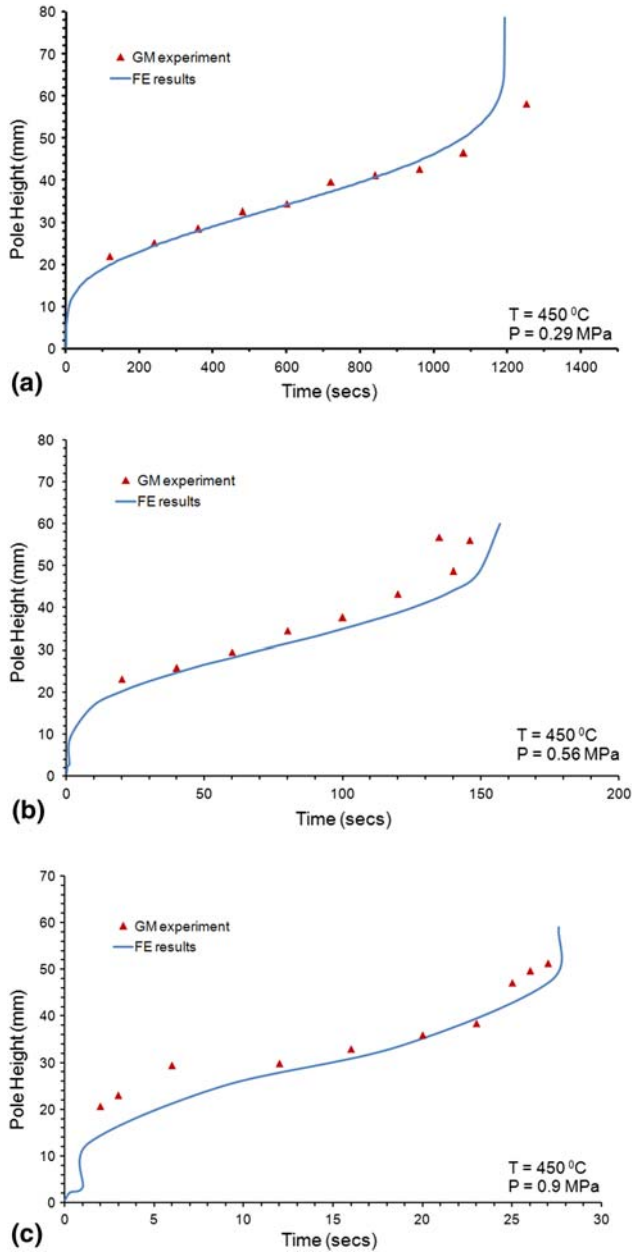

Fig. 6 Evolution of dome pole height for AA5083 at 450 °C for FE model (solid line) and GM experiment (triangles): (a) 0.29 MPa (42 psi), (b) 0.56 MPa (81 psi), and (c) 0.90 MPa (130 psi)

Figure 5(a)-(c) shows predicted incremental effective strain rate (s^{-1}) evolution at the dome pole for constant gas pressures of 0.29, 0.56, and 0.90 MPa, respectively. The incremental strain rate is $\ln(w_i/w_{i-1})/(t_i - t_{i-1})$, where i and $i-1$ are the current and the previous calculation steps in time, respectively, and w represents the sheet thickness. In general, the incremental strain rates are large at small forming times as the radius of curvature of the sheet changes rapidly, but then decrease to a minimum value as the bulge approaches a fully hemispherical geometry. At longer forming times, the incremental strain rates once again increase due to increased thinning at the dome pole. Comparison of Fig. 5(a)-(c) shows that the nominal incremental strain rate increases with forming pressure, as expected.

Figure 6(a)-(c) shows the FE-predicted dome pole height evolution at the same three gas pressures (solid curves). The triangles correspond to experimental AA5083 data from interrupted bulge tests detailed in Ref 3. Figure 7 shows the dome pole thickness evolution at the same pressures considered in Fig. 6. The phenomenological model, Eq 1-3, leads to FE predictions that closely follow the experimental trends in Fig. 6 and 7. This is due to its incorporation of the strain dependence of d, and the strain rate dependence of K and p at all strain rates considered in Fig. 2.

4.2 Bulge Forming with ABAQUS™ Pressure Control

Bulge forming simulations were run for $\dot{\bar{\varepsilon}}_{tar} = 0.0005$, 0.001, 0.005, 0.01, and 0.03 s^{-1} using the ABAQUS™ pressure

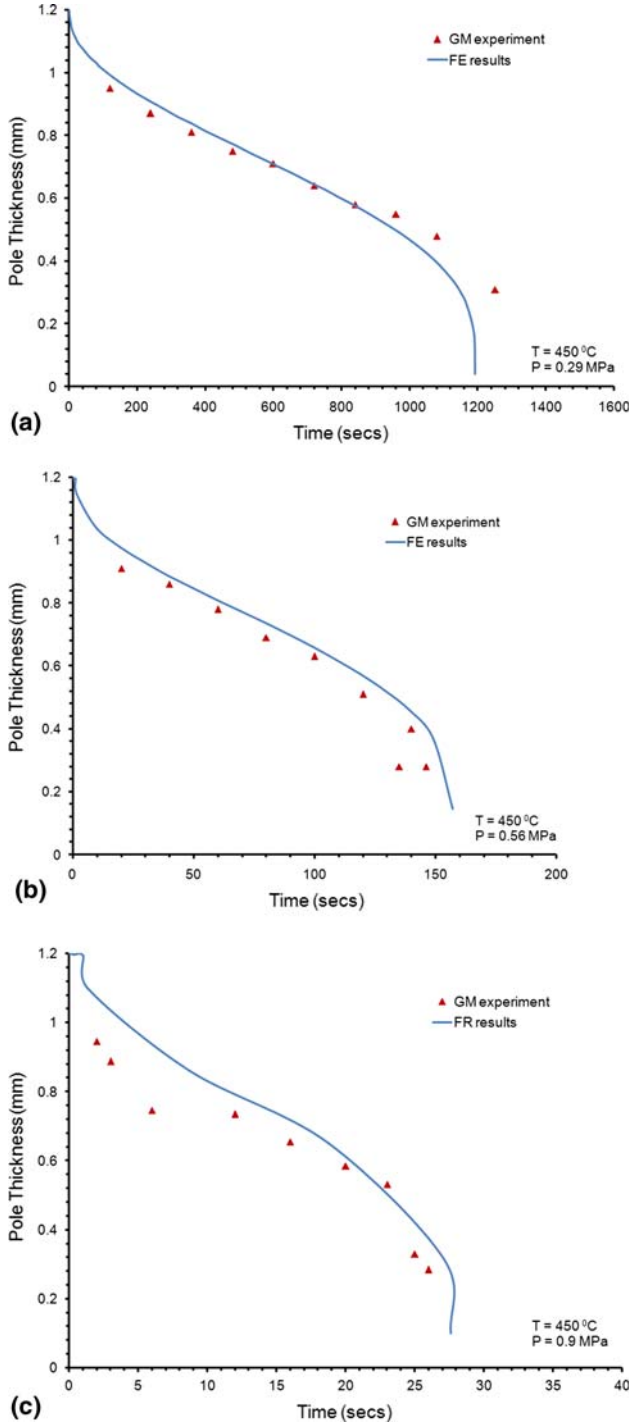

Fig. 7 Evolution of dome pole thickness for AA5083 at 450 °C for FE model (solid line) and GM experiment (triangles): (a) 0.29 MPa (42 psi), (b) 0.56 MPa (81 psi), and (c) 0.90 MPa (130 psi)

control routine detailed in Section 3. Figure 8 shows the evolution of the target strain rate ratio, r (see Eq 4), and resulting pressure profiles (in MPa) for small and large target dome pole strain rates of $\dot{\bar{\varepsilon}}_{tar} = 0.0005$ and 0.03 s^{-1}, respectively. Each curve is actually a set of discrete solution values that evolve according to the ABAQUS™ time step. A greater number of values were computed for the lower strain rate due to the time step size used in the FE calculations. This is the reason why the curves look contiguous rather than discrete. Fewer points are shown at the higher strain rates due to the step used in the associated calculations.

Note that r changes in response to the value of $\dot{\bar{\varepsilon}}_{max}$ at the dome pole at the current FE time step. Oscillations in r appear at the earliest stages of forming (t = 0-100 s). In Fig. 8(a), the pressure algorithm quickly ramps the gas pressure in a stepwise fashion in an attempt to maintain $\dot{\bar{\varepsilon}}_{tar} = 0.0005$ s^{-1} at the dome pole. Each stepwise change in r results from a corresponding stepwise change in the gas pressure. For example, at t = 250 s, r jumps from 0.8 to just above 1.2 to increase the forming rate after detecting a value of $\dot{\bar{\varepsilon}}_{max}$ that is too small at this time. Following this, r decreases smoothly until t = 525 s during which time the gas pressure maintains a constant value that just exceeds 0.2 MPa. Note that fluctuations in r are less rapid at this point as are the stepwise changes in the gas pressure since the forming process has moved beyond its earliest stages where the flat sheet develops curvature and hence adopts a dome shape. For t = 525-1125 s, the pressure remains constant at 0.28 MPa, while r decreases slightly and then increases, only to suddenly decrease at t = 1150 s in order to slow the rate of deformation at the dome pole. It is within this time of constant pressure that the behavior of the algorithm changes from one where r decreases following a step change, to one where r increases following a step change. For example, at t = 1150 s, the dome pole displacement is nearly 40.0 mm and the algorithm responds by decreasing the pressure to slow the deformation rate. A gradual increase in r is noted until t = 1600 s, where it once again drops corresponding to a drop in the gas pressure.

Figure 8(b) shows the variable pressure profile for $\dot{\bar{\varepsilon}}_{tar} = 0.03$ s^{-1} and hence a faster forming rate than that considered in Fig. 8(a). The range of r values beyond the very earliest forming stages where the flat sheet develops curvature is comparable to those in Fig. 8(a). Recall that the pressure algorithm does not target an average r value of 1.0; rather, it targets a range of r values (i.e. 0.8-1.5), and so as long as r falls within this range, the algorithm maintains the gas pressure. Note that the characteristic U-shaped profile in the effective strain rate noted in Fig. 5 appears in Fig. 8(a) and (b) as well. However, due to the stepwise changes in the applied pressure, the U-shape is cut into pieces and its pieces are shifted in the vertical direction.

Figure 9 shows dome pole height and thickness evolution for $\dot{\bar{\varepsilon}}_{tar} = 0.0005$ and 0.03 s^{-1} up to a dome height of 50 mm. No experimental data exist for comparison with the results in Fig. 9. However, these predictions could in fact be validated against data generated from experimental bulge tests wherein the gas pressure profiles follow those in Fig. 8. Total forming time, dome pole thickness, dome pole thickness strain, and thinning factor from the constant and variable pressure calculations are summarized in Table 2. The thinning factor is defined as the pole thickness divided by the average dome thickness (the average dome thickness is measured along a cross section contour, cutting the dome into two equal halves through the pole). A thinning factor of 1.0 means a perfect uniform thickness distribution. The lower the value of the thinning factor, the greater is the deviation in the thickness distribution (i.e. all along the bulge profile). A higher (constant) gas pressure leads to faster forming but greater thinning of the dome. A similar observation applies with a specified $\dot{\bar{\varepsilon}}_{tar}$, i.e., as $\dot{\bar{\varepsilon}}_{tar}$ increases, forming is faster but thinning is greater.

No advantage over P = 0.290 MPa is offered by the variable pressure forming where $\dot{\bar{\varepsilon}}_{tar} = 0.001$ s^{-1}. However, similar

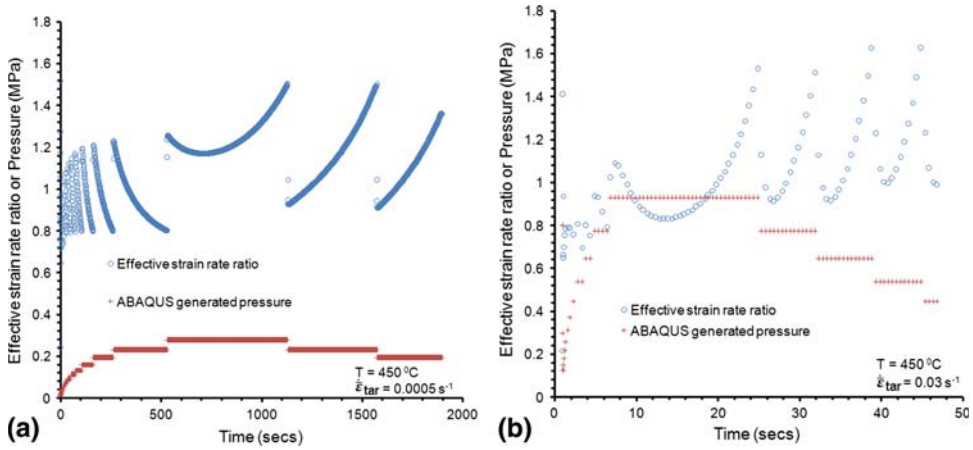

Fig. 8 Computed gas pressure profile ('+') and strain rate ratio ('○') from Eq 4 for target strain rate of (a) 0.0005 s^{-1} at the dome pole and (b) 0.03 s^{-1} at the dome pole

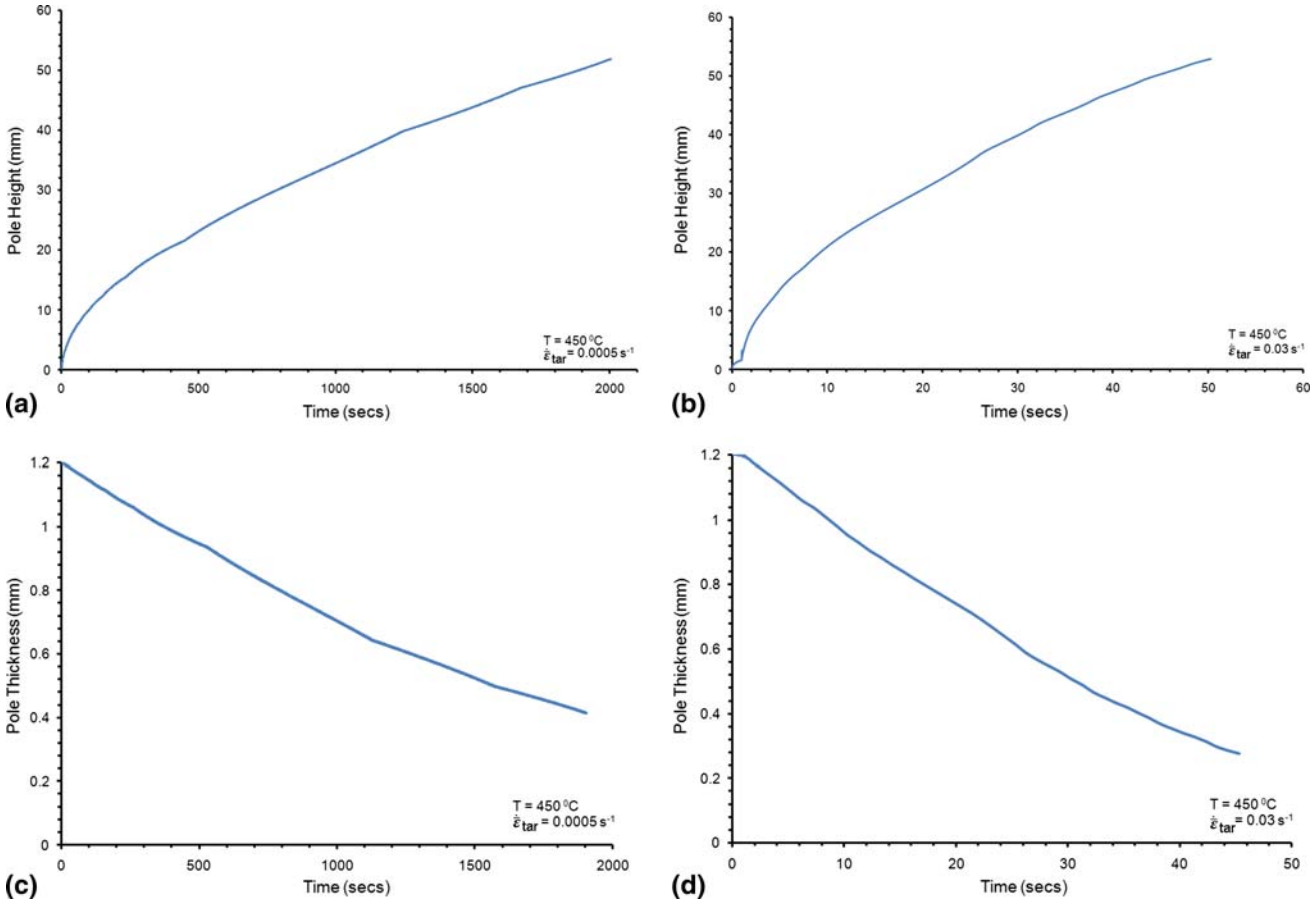

Fig. 9 Predictions from ABAQUS™ pressure control algorithm for AA5083 at 450 °C. Evolution of dome pole height at target strain rates of (a) 0.0005 s^{-1} and (b) 0.03 s^{-1}. Evolution of dome pole thickness at target strain rates of (c) 0.0005 s^{-1} and (d) 0.03 s^{-1}

pole thickness and thinning factors were achieved for the $P = 0.56$ MPa constant pressure and variable pressure forming resulting from $\dot{\bar{\varepsilon}}_{tar} = 0.01\ s^{-1}$. Variable pressure forming for $\dot{\bar{\varepsilon}}_{tar} = 0.01\ s^{-1}$ resulted in more rapid forming with a 28 s savings relative to the 152 s associated with a 0.56 MPa constant pressure.

The results in Table 2 suggest that an automatically varying pressure based on a target strain rate may have a potential advantage, in terms of forming time and thinning, over using a constant pressure forming. However, experimental validation of the time-varying pressure forming results is still required.

Table 2 Quantities predicted with the different loading paths in bulge forming of AA5083 at 450 °C

Pressure loading	Forming time to 50.0 mm dome pole displacement, s	Dome pole thickness, mm	Dome pole thickness strain	Thinning factor
P = 0.29 MPa (42 psi)	1078	0.40	1.11	0.62
P = 0.56 MPa (81 psi)	152	0.33	1.29	0.50
P = 0.90 MPa (130 psi)	27	0.25	1.57	0.36
$\dot{\bar{\varepsilon}}_{tar} = 0.0005\ s^{-1}$	1900	0.42	1.06	0.64
$\dot{\bar{\varepsilon}}_{tar} = 0.001\ s^{-1}$	1074	0.40	1.10	0.62
$\dot{\bar{\varepsilon}}_{tar} = 0.005\ s^{-1}$	241	0.35	1.23	0.53
$\dot{\bar{\varepsilon}}_{tar} = 0.01\ s^{-1}$	124	0.33	1.31	0.49
$\dot{\bar{\varepsilon}}_{tar} = 0.03\ s^{-1}$	47	0.28	1.45	0.42

Initial sheet thickness = 1.2 mm. Thinning factor = pole thickness divided by the average dome thickness

5. Concluding Remarks

High-temperature bulge forming of AA5083 under quick plastic forming conditions was simulated with constant pressure profiles from experiments. A high-temperature material model fit to tensile data over a wide range of strain rates was developed for input to the commercial FE code ABAQUS™. The close accord between experimentally determined pole height and thickness evolution profiles and FE simulation results demonstrate the importance of including material hardening/softening in the AA5083 material model. In ancillary calculations, a strain rate control algorithm internal to ABAQUS™ was used to compute gas pressure profiles based upon a user-selected target creep strain rate ($\dot{\bar{\varepsilon}}_{tar}$) at the dome pole. As was the case with the constant pressure results, a higher gas pressure leads to faster forming but greater thinning of the dome. For pressures of 0.29 and 0.56 MPa, equal or better forming results were obtained using constant strain rate simulations ($\dot{\bar{\varepsilon}}_{tar}$ = 0.001 and 001 s^{-1}, respectively). For 0.9 MPa, forming using a target effective strain rate larger than 0.03 s^{-1} would likely provide equal or better forming results.

Clearly, the opportunity exists to improve upon the ABAQUS™ strain rate control algorithm with one that leads to a smooth rather than stepwise variation in the pressure profile. In fact, such an improvement was detailed in Ref 28 for a material model that is inappropriate for high-temperature AA5083 forming under QPF conditions. More sophisticated gas pressure control algorithms that can detect the onset of local sheet thinning/necking (and possibly damage) at multiple points in the sheet should be developed for FE simulations of QPF processes. Such algorithms will quickly adjust the gas pressure so as to avoid premature sheet failure in QPF while maintaining or improving upon existing part cycle times.

Acknowledgment

The financial support of the National Science Foundation, CAREER award # DMI-0238712 and General Motors Corporation (GM) is greatly appreciated.

References

1. X.D. Ding, H.M. Zbib, C.H. Hamilton, and A.E. Bayoumi, On the Stability of Biaxial Stretching with Application to the Optimization of Superplastic Blow-Forming, *J. Eng. Mater. Technol.*, 1997, **119**, p 26–31
2. K. Siegert and S. Jaeger, Pneumatic Bulging of AZ31 Sheet Metal at Elevated Temperatures, *Magnesium Technology 2004*, A.A. Luo, Ed., The Minerals, Metals & Materials Society (TMS), 2004, p 87–90
3. J.R. Bradley, Bulge Testing of Superplastic AA5083 Aluminum Sheet, *Advances in Superplasticity and Superplastic Forming*, E.M. Taleff, P.A. Friedman, P.E. Krajewski, R.S. Mishra, and J.G. Schroth, Eds., March 14-18, 2004 (Charlotte, North Carolina, USA), The Minerals, Metals & Materials Society (TMS), 2004, p 109–118
4. D.M. Woo, The Analysis of Axisymmetric Forming of Sheet Metal and the Hydrostatic Bulging Process, *Int. J. Mech. Sci.*, 1964, **6**, p 303–317
5. F. Jovane, An Approximate Analysis of the Superplastic Forming of a Thin Circular Diaphragm: Theory and Experiments, *Int. J. Mech. Sci.*, 1968, **10**, p 403–427
6. G.C. Cornfield and R.H. Johnson, The Forming of Superplastic Sheet Metal, *Int. J. Mech. Sci.*, 1970, **12**, p 479–490
7. S.W. Chung, K. Higashi, and W.J. Kim, Superplastic Gas Pressure Forming of Fine Grained AZ61 Magnesium Alloy Sheet, *Mater. Sci. Eng.*, 2004, **372**, p 15–20
8. M. Atkinson, Accurate Determination of Biaxial Stress-Strain Relationships from Hydraulic Bulging Tests of Sheet Metals, *Int. J. Mech. Sci.*, 1997, **39**, p 761–769
9. D. Banabic, M. Vulcan, and K. Siegert, Bulge Testing Under Constant and Variable Strain Rates of Superplastic Aluminium Alloys, *CIRP Ann. Manuf. Technol.*, 2005, **54**, p 205–208
10. S.N. Patankar and T.M. Jen, Superplastic Forming of Commercial Purity Aluminum, *Scr. Mater.*, 1997, **38**, p 145–148
11. Y. Luo, C. Miller, G. Luckey, P. Friedman, and Y. Peng, On Practical Forming Limits in Superplastic Forming of Aluminum Sheet, *J. Mater. Eng. Perform.*, 2007, **16**(3), p 274–283
12. P.E. Krajewski and J.G. Schroth, Overview of Quick Plastic Forming, *Mater. Sci. Forum*, 2007, **551-552**, p 3–12
13. ABAQUS™: www.simulia.com
14. ABAQUS™ Analysis User's Manual, Vol. 3, Version 6.5, 2004, p 11.2.4-10
15. P.E. Krajewski and G.P. Montgomery, Mechanical Behavior and Modeling of AA5083 at 450°C, *Advances in Superplasticity and Superplastic Forming*, E.M. Taleff, P.A. Friedman, P.E. Krajewski, R.S. Mishra, and J.G. Schroth, Eds., March 14-18, 2004 (Charlotte, North Carolina, USA), The Minerals, Metals & Materials Society (TMS), 2004, p 341–350
16. M.K. Khraisheh and F.K. Abu-Farha, Microstructure-Based Modeling of Anisotropic Superplastic Deformation, *Trans. NAMRI/SME*, 2003, **31**, p 41–47
17. M.N. Nazzal, M.K. Khraisheh, and B. Darras, Finite Element Modeling and Optimization of Superplastic Forming Using Variable Strain Rate Approach, *J. Mater. Eng. Perform.*, 2004, **13**(6), p 691–699
18. F.K. Abu-Farha and M.K. Khraisheh, Analysis of Superplastic Deformation of AZ31 Magnesium Alloy, *J. Adv. Eng. Mater.*, 2007, **9**(9), p 777–783
19. C.H. Caceres and D.S. Wilkinson, Large Strain Behavior of a Superplastic Copper Alloy-Deformation, *Acta Metall.*, 1984, **32**, p 415–422
20. M.J. Stowell, Cavity Growth and Failure in Superplastic Alloys, *Met. Sci.*, 1983, **17**, p 92–98

21. C.L. Chen and M.J. Tan, Cavity Growth and Filament Formation of Superplastically Deformed Al 7475 Alloy, *Mater. Sci. Eng. A*, 2001, **298**, p 235–244
22. Y. Chino and H. Iwasaki, Cavity Growth Rate in Superplastic 5083 Al and AZ31 Mg Alloys, *J. Mater. Res.*, 2004, **19**(11), p 3382–3388
23. F. Li, D.H. Bae, and A.K. Ghosh, Grain Elongation and Anisotropic Grain Growth During Superplastic Deformation in an Al-Mg-Mn-Cu Alloy, *Acta Mater.*, 1997, **45**(9), p 3887–3895
24. M.A. Khaleel, M.T. Smith, and A.L. Lund, Cavitation During Multiaxial Deformation of Superplastic Forming, *Mater. Sci. Forum*, 1997, **243-245**, p 155–160
25. E. Tanaka, S. Murakami, and H. Ishikawa, Constitutive Modeling of Superplasticity Taking Account of Grain and Cavity Growth, *Mater. Sci. Forum*, 1997, **233-234**, p 21–28
26. H. Iwasaki, T. Mori, T. Tagata, M. Masatu, and K. Higashi, Cavitation in Superplastic Al-Mg Alloy, *Mater. Sci. Forum*, 1997, **233-234**, p 81–88
27. S.C. Rama and N. Chandra, Development of a Pressure Prediction Method for Superplastic Forming Processes, *Int. J. Non-Linear Mech.*, 1991, **26**, p 711–725
28. S.G. Luckey, P.A. Friedman, and Z.C. Xia, Aspects of Element Formulation and Strain Rate Control in the Numerical Modeling of Superplastic Forming, *Advances in Superplasticity and Superplastic Forming*, E.M. Taleff, P.A. Friedman, P.E. Krajewski, R.S. Mishra, and J.G. Schroth, Eds., March 14-18, 2004 (Charlotte, North Carolina, USA), The Minerals, Metals & Materials Society (TMS), 2004, p 371–380
29. H. Samekto and K. Roll, Finite Element Analysis of Superplastic Forming Process Using LS-DYNA, 4th European LS-DYNA Users Conference, May 22-23, 2003 (Ulm, Germany), DYNA*more*, 2003, p E-11-01–E-11-16